PAPER

Check for updates

Atomically precise bismuth oxido nanoclusters: cerium doping for optical modification and supramolecular self-assembly on Au(111)†

Rico Thomas, [ID] [a] Thi Ngoc Ha Nguyen, [ID] [b] Marcus Weber, [ID] [a,c] Tobias Rüffer, [ID] [d] Fabian Göhler, [ID] [c,e] Antareekshya Deka, [ID] [f] Andreas Pöppl, [ID] [f] Thomas Seyller, [ID] [e] Christoph Tegenkamp [ID] [b] and Michael Mehring [ID] *[a,c]

The functionalization of atomically precise bismuth oxido nanoclusters (BiO-NCs) by partial substitution of bismuth with cerium, chiral modification by ligand substitution, and their 2D-supramolecular self-assembly on surfaces such as Au(111) and HOPG(0001) was studied. Starting from $[Bi_{38}O_{45}(NO_3)_{20}(dmso)_{28}]$ $(NO_3)_4 \cdot 4dmso$ (**C-1**) and its cerium doped counterpart $[Bi_{38}O_{45}(NO_3)_{24}(dmso)_{28}]:Ce \cdot 1.5dmso$ (**C-1:Ce**), soluble BiO-NCs with a size of 2 nm are obtained by reaction with methacrylate and chiral carboxylates to give $[Bi_{38}O_{45}(L)_{24}]$ and $[Bi_{38}O_{45}(L)_{24}]:Ce$ with L = McO⁻ (**C-2** and **C-2:Ce**), Boc-ʟ-Phe−O⁻ (**C-3** and **C-3:Ce**), and Boc-ʟ-Ala−O⁻ (**C-4** and **C-4:Ce**). The cerium doping content determined using ICP-OES and the oxidation state of cerium determined *via* XP- and EPR spectroscopy were studied, showing Ce(III) for the carboxylate functionalized BiO-NCs, whereas mixed valency Ce(III)/Ce(IV) was detected for the nitrate **C-1: Ce**. However, doping of BiO-NCs with cerium results in a change of absorption from the UV to the visible light region for all compounds, whereby the red-shift is concluded to originate from the MLCT from Ce(III) to oxygen. The self-assembly of chiral BiO-NCs $[Bi_{38}O_{45}(Boc-ʟ-Phe-O)_{24}]$ (**C-3**) and $[Bi_{38}O_{45}(Boc-ʟ-Phe-O)_{24}]:Ce$ (**C-3:Ce**) on Au(111) and HOPG(0001) was analyzed. STM images of BiO-NCs revealed a stepwise one-dimensional arrangement of BiO-NCs and STS analysis proved significant changes in the electronic energy gap as a result of ≈1 ω% Ce(III) doping (**C-3** E_g = 3.5 eV *vs.* **C-3:Ce** E_g = 2.6 eV).

Introduction

Since the famous lecture of Richard P. Feynman "There's Plenty of Room at the Bottom" at the annual meeting of the American Physical Society in 1959, nanoscience has become one of the most important research fields leading to novel technologies based on the use of nanoparticles (NPs).[1] Starting from that, one of the major challenges was the targeted synthesis of NPs having defined and uniform composition, size and shape, allowing precise tuning of the physical properties. Among the numerous synthetic protocols that were developed, those that provide monodisperse NPs have to be highlighted.[2–4] Physical and chemical properties are even better defined for atomically precise nanoclusters (NCs) and thus, research on NCs of metals and alloys came more and more into focus.[5–8] Even though the synthesis of NCs needs sophisticated experimental methods, they provide a highly reproducible way to study the size-dependent properties. Such NCs with sizes of a few nanometers represent the link between molecules and nanoparticles, and they can be studied by methods of molecular chemistry such as single crystal X-ray diffraction (SC XRD), nuclear magnetic resonance (NMR) and mass spectrometry (MS) in addition to methods commonly applied to nanoparticles. Thus, either the influence of the core atoms or the ligand shell on the electronic structure or surface reactivity can be studied with molecular precision. In addition to the intensively studied metal- and metalloid-based NCs, metal sulfide and selenide NCs have attracted increasing interest in the past. Less attention has

[a] Faculty of Natural Science, Institute of Chemistry, Coordination Chemistry, Chemnitz University of Technology, Straße der Nationen 62, 09107 Chemnitz, Germany. E-mail: michael.mehring@chemie.tu-chemnitz.de

[b] Faculty of Natural Science, Institute of Physics, Analysis of Solid Surfaces, Chemnitz University of Technology, Straße der Nationen 62, 09107 Chemnitz, Germany

[c] Center of Materials, Architectures and Integration of Nanomembranes, Chemnitz University of Technology, Rosenbergstraße 6, 09126 Chemnitz, Germany

[d] Faculty of Natural Science, Institute of Chemistry, Inorganic Chemistry, Chemnitz University of Technology, Straße der Nationen 62, 09107 Chemnitz, Germany

[e] Faculty of Natural Science, Institute of Physics, Technical Physics, Chemnitz University of Technology, Straße der Nationen 62, 09107 Chemnitz, Germany

[f] Faculty of Physics and Earth System Science, Felix-Bloch-Institute for Solid State Physics, Technical Physics, University of Leipzig, Linnéstraße 5, 04103 Leipzig, Germany

†Electronic supplementary information (ESI) available: Experimental details, material characterization and extended analysis. CCDC 2386322 and 2386323. For ESI and crystallographic data in CIF or other electronic format see DOI: https://doi.org/10.1039/d5nr02346g

been paid to nanosized metal oxido NCs (MO-NCs) other than polyoxometalates (POMs), which constitute a well-established, unique class of materials composed of negatively charged species and diverse counter cations. In contrast, the neutral MO-NCs, as reported here, strongly resemble cut-outs of the parent metal oxide.[9–20]

Bismuth oxido nanoclusters (BiO-NCs) play a special role within the class of MO-NCs due to their structural diversity and first reports towards applications in transparent radiopaque materials, photocatalysis, energy storage and rewritable resistive memory devices were published.[21–24] The cationic $[Bi_{38}O_{45}]^{24+}$ framework has been referred to as a 'magic cluster', which is characterized by high stability and the ability to attach diverse anionic moieties.[22,25–35] Moreover, we have recently reported on a doped MO-NC prepared by the substitution of bismuth with cerium within the cluster core, $[Bi_{38}O_{45}(NO_3)_{24}(dmso)_{28}]$: Ce·1.5dmso (**C-1:Ce**).[36] NCs with variations in the occupancy of the dopant are studied intensely for metal-NCs,[5,37–39] but doping in MO-NCs has not caught similar attention and is mainly restricted to titanium oxido clusters.[40–43]

Cerium is one of the few lanthanides that has two stable oxidation states, Ce(III/IV), which often leads to the occurrence of mixed valence cerium compounds as observed in various cerium oxido nanoclusters.[11,44,45] Even for CeO_2, a Ce(III) content up to 5% is found to be present, primarily placed at the surface in combination with oxygen deficiency.[46,47] We thus have a MO-NC at hand that allows us to study the effects of doping with molecular precision, which in turn should provide further insight into metal oxide doping in a more general view. The first example was published recently (**C-1:Ce**), however leaving open questions on its mixed valent nature. We did also face the problem of restricted solubility of the bismuth oxido nitrate cluster, which hampers controlled deposition of BiO-NCs on surfaces for further analysis and application. As demonstrated for a homometallic BiO-NC functionalized with an N-(tert-butoxycarbonyl)-L-phenylalanine (Boc-L-Phe-O⁻) ligand shell, the solubility can be significantly enhanced and thin film deposition becomes possible.[25]

Here, we report on the combination of doping and ligand exchange, and provide insight into the oxidation state of cerium in combination with the effect of the bonded ligands methacrylate (McO⁻), Boc-L-Phe–O⁻, and N-(tert-butoxycarbonyl)-L-alanine (Boc-L-Ala–O⁻) and on the optical and electronic properties of the BiO-NCs. In addition, the influence of doping on the self-assembly process of BiO-NCs on Au(111) and pyrolytic graphite HOPG(0001) was studied using scanning tunneling microscopy (STM) and scanning tunneling spectroscopy (STS). The combination of both techniques allows simultaneous obtention of information on both topography and electrical properties of NCs on surfaces.[48–53]

Results and discussion

For the synthesis of the novel carboxylate functionalized, undoped and cerium doped BiO-NCs, the previously reported

BiO-NCs $[Bi_{38}O_{45}(NO_3)_{20}(dmso)_{28}](NO_3)_4\cdot4dmso$ (**C-1**)[54] and $[Bi_{38}O_{45}(NO_3)_{24}(dmso)_{28}]$:Ce (**C-1:Ce**) were prepared using a modified procedure.[36] Starting from **C-1** and **C-1:Ce**, the BiO-NCs of the composition $[Bi_{38}O_{45}(L)_{24}]$ and $[Bi_{38}O_{45}(L)_{24}]$: Ce (L = McO⁻ (**2**); **C-2, C-2:Ce**; L = Boc-L-Phe–O⁻ (**3**); **C-3, C-3: Ce**; and L = Boc-L-Ala–O⁻ (**4**); **C-4, C-4:Ce**, Fig. 1a) were prepared by reaction with the respective sodium carboxylates. Table S1† summarizes the chemical formula of all synthesized compounds. The homometallic BiO-NCs (**C-2, C-3**, and **C-4**) were obtained as colorless crystalline materials, whereas yellow-colored crystalline compounds were formed in the case of cerium doped BiO-NCs (**C-2:Ce, C-3:Ce**, and **C-4:Ce**).

BiO-NCs with a $\{Bi_{38}O_{45}\}$ core are built out of a central $\{Bi_6O_9\}$ unit, surrounded by 12 edge sharing $[Bi_6O_{8-x}]^{2(1+x)+}$ octahedra. The fcc packing of the bismuth atoms in the cluster core with a fully occupied oxygen sublattice is related to the solid-state structures of β-Bi_2O_3 and δ-Bi_2O_3.[55] Furthermore, the $\{Bi_{38}O_{45}\}$ cluster core is covered by the coordinating ligand sphere. The doping of the cluster with cerium results in the statistical occupancy of some bismuth(III) positions, where the rare earth metal cation primarily favors the inner $\{Bi_6O_9\}$ core motif and neighboring Bi positions in the NC. The crystalline material is best described as a mixture of doped BiO-NCs with one cerium $\{Bi_{37}CeO_{45}\}$ as a majority compound and of undoped BiO-NCs $\{Bi_{38}O_{45}\}$. The bond lengths and angles within the nanocluster, as well as the coordinated ligand are only slightly affected by the doping.[36] This holds true for the novel methacrylate substituted, doped BiO-NC **C-2:Ce**, which shows similar structural parameters as reported for **C-2** (Fig. 1a)[22] and is discussed in more detail in the ESI (cf. Tables S2 and S4†). The determination of the occupancy of the cerium atoms within the cluster is important for the structure description of the cerium doped clusters. In the case of BiO-NC **C-2:Ce**, four positions are partially occupied by cerium (cf. Fig. 1b). In **C-1:Ce**, eight different positions are occupied. In both clusters, the positions in the central $\{Bi_6O_9\}$ unit of the bismuth oxido core are occupied predominantly. Interestingly, the relative occupancy rate of these positions, ranging from 8.6 (7)% to 12.0(7)% (**C-2:Ce**, cf. Table S3†), is significantly higher as compared to **C-1:Ce** (occupancy factors from 1.9(9)% to 6.6 (9)%). We assume that the difference results from the modified reaction conditions and/or the adoption of different space groups (**C-1:Ce** in C2/c; **C-2:Ce** in P$\bar{1}$). Overall, a dopant content of 0.336 cerium atoms per $\{Bi_{38}O_{45}\}$ unit was determined for the crystal structure of **C-2:Ce** (**C-1:Ce** 0.28 per unit), which accounts for total cerium contents of 0.32 ω% (**C-1:Ce**)[36] and 0.41 ω% (**C-2:Ce**). The cerium content measured with ICP-OES of the as-synthesized **C-1:Ce** with 1.10 ω% is increased compared to the previously published results with 0.69 ω% (ICP-OES). In **C-2:Ce**, the cerium content determined using ICP-OES (0.31 ω%) is in good agreement with the results from SC XRD (0.41 ω%). The Boc-amino acid anion coordinated and cerium doped BiO-NCs revealed slightly higher dopant contents compared to **C-2:Ce**, with 0.73 ω% (**C-3:Ce**) and 1.00 ω% (**C-4:Ce**). Please note that about 30% (**C-2:Ce**), 65% (**C-3:Ce**) and 83% (**C-4:Ce**) of the BiO-NCs are doped with at least one
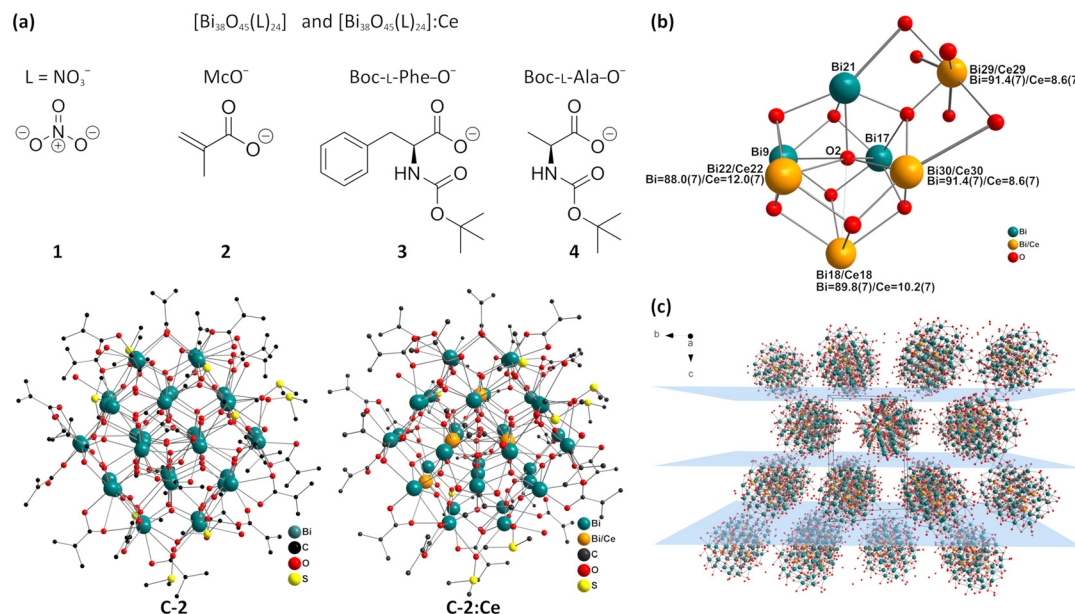
Fig. 1 (a) General chemical composition of homometallic and cerium doped BiO-NCs with the formula of the corresponding carboxylate ligands below. "Ball and stick" model based on the SC XRD structural data of homometallic BiO-NC **C-2** and cerium doped BiO-NC **C-2:Ce**. Hydrogen atoms are omitted for clarity. (b) "Ball and stick" model of the selected part of BiO-NC **C-2:Ce** showing the central [Bi/Ce$_6$O$_9$] polyhedron with the adjusted (Bi29/Ce29) including the occupancy parameters of Bi/Ce in %. (c) Section of the solid-state structure of **C-2:Ce** to visualize the packing of BiO-NCs; view along the a-axis with highlighted lattice planes (001) and (002). Hydrogen, sulfur and carbon are omitted for clarity.

cerium. Noteworthily, the as-prepared crystalline compounds consist of both homo- and heterobimetallic BiO-NC species, which is confirmed by the mass spectrometric detection of the respective BiO-NC cations in the gas phase generated from electrosprayed compounds **C-2:Ce**, **C-3:Ce** and **C-4:Ce** (see the discussion on ESI-MS).

In the solid state, the BiO-NCs are arranged in a hexagonal close packing (Fig. 1c). This is reflected in the resulting powder X-ray diffraction (PXRD) pattern of the respective BiO-NCs (comp. Fig. S2†) from which the interlayer distance (and thus the diameter) can be calculated from the major diffraction at low 2θ values (comp. Table S5†).[25] Overall, the cerium doped and undoped BiO-NCs show similar PXRD patterns and a similar main diffraction 2θ range, indicating that cerium does not influence the size of the {Bi$_{38}$O$_{45}$} core. The clusters **C-1**, **C-1:Ce** and **C-2**, **C-2:Ce** with nitrate and methacrylate ligands show a diameter of about 1.7 nm, while the clusters **C-3**, **C-3:Ce** and **C-4**, **C-4:Ce** with the larger amino acid ligands show a diameter of about 1.9 nm. Furthermore, the PXRD patterns of **C-1**, **C-1:Ce** and **C-2**, **C-2:Ce** are in good accordance with those calculated from the corresponding SC XRD data (*cf.* Fig. S3†). Thus, an intact BiO-NC structure in the solid state is concluded for all as-prepared compounds.

ESI-MS has proven to be a powerful analytical tool for determining the chemical composition of single BiO-NCs.[36,56,57] In the case of the cerium doped compounds, {Bi$_{38-x}$Ce$_x$O$_{45}$} species containing one Ce atom in **C-1:Ce** are dominating,[36] but up to two Ce atoms in **C-2:Ce**, one Ce atom in **C-3:Ce**, and up to three Ce atoms for **C-4:Ce** were detected in the gas phase next to the homometallic species based on the [Bi$_{38}$O$_{45}$]$^{24+}$

motif. The presence of only Ce(III) doped BiO-NC cations with lower abundance with regard to dominant [Bi$_{38}$O$_{45}$]$^{24+}$ species is in line with previously reported ESI-MS studies on **C-1:Ce**,[36] concluding that the cerium oxidation state +IV is not stable in the gas phase of BiO-NCs coordinated with nitrate. Parts of the ESI mass spectra of Boc-alanine coordinated BiO-NCs **C-4**, and **C-4:Ce** are shown exemplarily (Fig. 2). Survey ESI mass spectra and selected parts of the spectra as well as assigned species for all other BiO-NCs are given and discussed in the ESI (Fig. S4–S13 and Tables S6–S10†), confirming the complete ligand exchange. Applying soft ionization conditions, typical charge states of doubly, triply, and quadruply positive charged BiO-NCs cations were generated by stripping off the appropriate number of counter anions.[54] The ESI-MS spectra of **C-4** and **C-4:Ce**, allow a reliable assignment of both homo- and heterobimetallic cationic species (Tables S9 and S10†). Both spectra are dominated by the homometallic species [Bi$_{38}$O$_{45}$(Boc-L-Ala–O)$_{22}$]$^{2+}$ (**XXXVII**, m/z = 6400.5377), whereas the Ce doped species are present showing less abundant m/z signals. The MS of **C-4:Ce** allows the identification of several cerium doped species such as [Bi$_{37}$CeO$_{45}$(Boc-L-Ala–O)$_{22}$]$^{2+}$ (**XLIX**, major species), [Bi$_{36}$Ce$_2$O$_{45}$(Boc-L-Ala–O)$_{22}$]$^{2+}$ (**L**), and [Bi$_{35}$Ce$_3$O$_{45}$(Boc-L-Ala–O)$_{22}$]$^{2+}$ (**LI**) (Table S10†). In the case of **C-4:Ce**, ESI-MS reveals four different nanocluster cores with Bi/Ce compositions such as {Bi$_{38}$}, {Bi$_{37}$Ce}, {Bi$_{36}$Ce$_2$}, and {Bi$_{35}$Ce$_3$}, with the two latter representing minor species. In summary, the complete ligand modification in all BiO-NCs has been confirmed by ESI-MS analysis. Furthermore, the doped clusters show cerium doped fragments with up to three cerium in addition to undoped fragments.
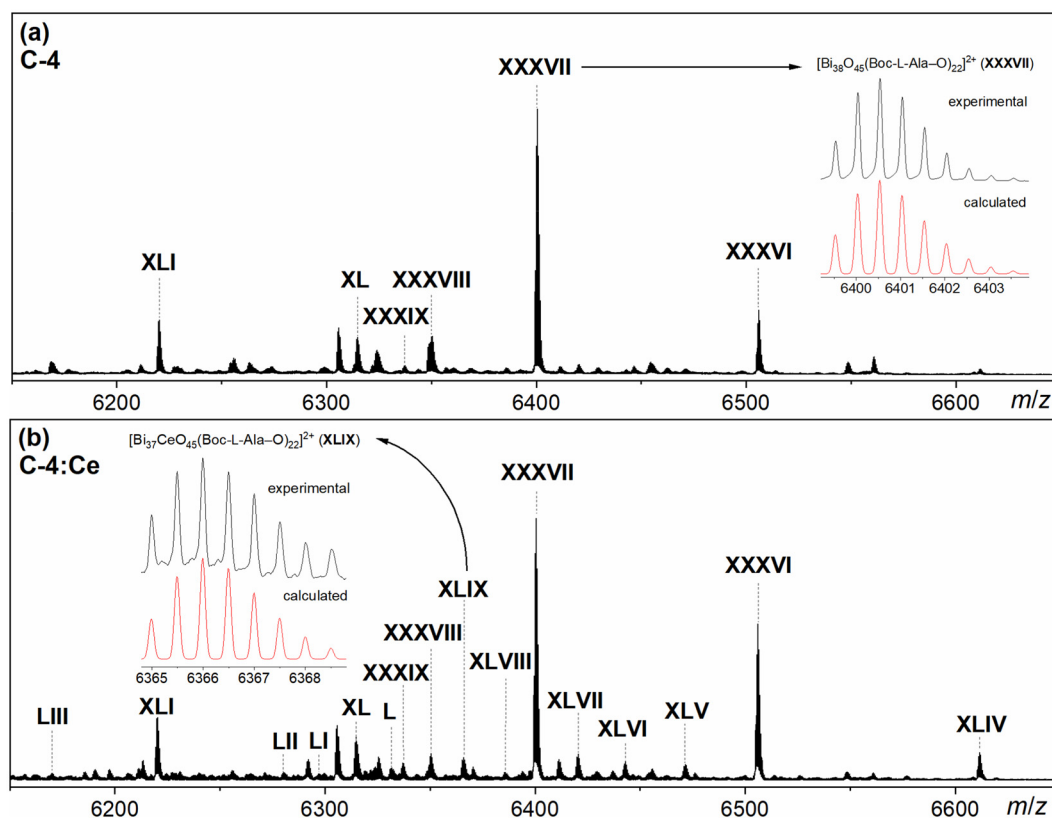
Fig. 2 (a) Part of the ESI mass spectrum of compound **C-4** electrosprayed from MeOH showing doubly positive charged homometallic bismuth oxido cluster cations (**XXXVI–XLI**); $[Bi_{38}O_{45}(Boc\text{-}L\text{-}Ala\text{-}O)_{22}]^{2+}$ (**XXXVII**) at $m/z = 6400.5377$ with the highest abundance. All labeled cations and their assignment are summarized in Table S9.† (b) Part of the ESI mass spectrum of compound **C-4:Ce** electrosprayed from MeOH showing doubly positive charged homometallic bismuth oxido cluster cations (**XXXVI–XLI**); $[Bi_{38}O_{45}(Boc\text{-}L\text{-}Ala\text{-}O)_{22}]^{2+}$ (**XXXVII**) at $m/z = 6400.5351$ showing the highest abundance. Several Ce doped BiO-NC cations (**XLV, XLVIII–LII**) with varying dopant contents were detected with low abundance. All labeled cations and their assignment are summarized in Table S10.†

In accordance with the ESI-MS results, Fourier transform infrared (FTIR) spectra of the as-prepared BiO-NCs confirm the complete substitution of nitrate by the carboxylate ligands in the cluster periphery (Table S11 and Fig. S14†). Most importantly, the absorption bands of the nitrate groups of the precursors **C-1** and **C-1:Ce** at around 1380 cm^{-1} ($\nu_{as.}(NO_2)$) and 1265 cm^{-1} ($\nu_{sym.}(NO_2)$) for bidentate nitrates, at 1430 cm^{-1} ($\nu_{as.}(NO_2)$) and 957 cm^{-1} ($\nu_{sym.}(NO_2)$) for monodentate nitrates and at approximately 1740 cm^{-1} for free nitrate[36,54] are no longer detected in the carboxylate substituted BiO-NCs.

The ^1H and ^{13}C NMR spectra of all BiO-NCs are in accordance with the chemical composition of the BiO-NCs assuming a homoleptic ligand shell with averaged coordination modes (Fig. S15–S20†). The signals in the NMR spectra of cerium doped and undoped nanoclusters did not reveal significant difference in their chemical shifts and peak widths. In agreement with IR spectroscopy, some residual DMSO is detected. Notably, the nitrate coordinated nanoclusters **C-1** and **C-1:Ce** are only soluble in DMSO, while the carboxylate coordinated BiO-NCs are soluble in various polar organic solvents, such as ethanol or acetonitrile. The Boc-phenylalanine modified BiO-NCs (**C-3/C-3:Ce**) exhibit a slightly higher solubility in

ethanol (≈ 75 g L^{-1}) compared to those coordinated by Boc-alanine ligands (**C-4/C-4:Ce**, ≈ 65 g L^{-1}). Therefore, the nanoclusters **C-3** and **C-3:Ce** represent the best suited candidates, from the as-prepared compounds, for the deposition experiments of single clusters on well-defined gold substrates.

CD spectroscopy demonstrated the introduction of the chiral information into Boc-protected amino acid anion coordinated BiO-NCs such as undoped **C-3**, $[Bi_{38}O_{45}(Boc\text{-}L\text{-}Met\text{-}O)_{24}]$ and $[Bi_{38}O_{45}(Boc\text{-}L\text{-}Val\text{-}O)_{22}(OH)_2]$.[26,58] The CD spectra of **C-3, C-3:Ce** (*cf.* Fig. S21a†) and **C-4, C-4:Ce** (*cf.* Fig. 3a) show the expected Cotton effects of the ligand centered signal (<225 nm) and a signal for the ligand induced charge transfer band (approx. 275 nm) confirming the presence of chiral BiO-NCs. Notably, the maxima are in a similar range compared to the absorption maxima of the respective UV–vis spectra at 275 nm (Fig. 5, Table S12†). Strikingly, the CD signal of the chiral clusters is not affected by cerium doping, as neither broadening nor shifting of the band for the chiral cluster is observed. Furthermore, cerium doping in the core $\{Bi_{38-x}Ce_xO_{45}\}$ does not lead directly to the presence of chiral BiO-NCs as no CD signals are observed for **C-2** and **C-2:Ce** (Fig. S22a†). We conclude that the optical signal for the chiral
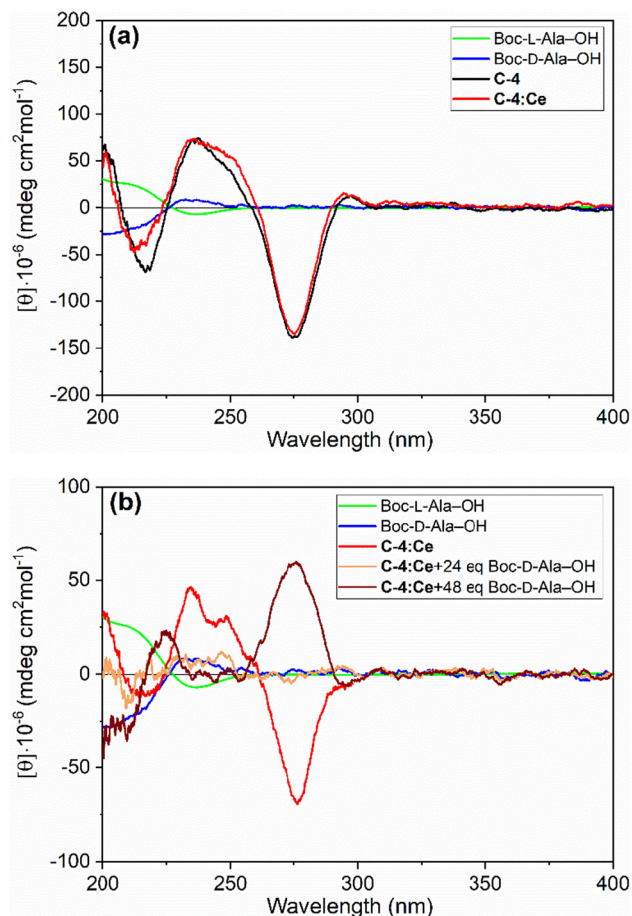
Fig. 3 CD spectra of Boc-L-alanine (green, $c = 1 \times 10^{-3}$ M), Boc-D-alanine (blue, $c = 1 \times 10^{-3}$ M), (a) BiO-NC **C-4** (black, $c = 5 \times 10^{-5}$ M) and BiO-NC **C-4:Ce** (red, $c = 5 \times 10^{-5}$ M) in acetonitrile and (b) CD spectra of BiO-NC **C-4:Ce** (red, $c = 5 \times 10^{-5}$ M), BiO-NC **C-4:Ce** + 24 eq. Boc-D-alanine (yellow, $c = 5 \times 10^{-5}$ M) and BiO-NC **C-4:Ce** + 48 eq. Boc-D-alanine (dark red, $c = 5 \times 10^{-5}$ M) in acetonitrile.

clusters is caused by a chiral ligand induced charge transfer process, which is however not significantly influenced by the nature of the coordinated amino acids.

CD spectroscopy was used to track the *in situ* ligand exchange reactions for **C-3:Ce** (*cf.* Fig. S21b†) and **C-4:Ce** (*cf.* Fig. 3b) in acetonitrile with the respective D-amino acid enantiomers added in an equimolar amount (24 eq.) and in excess (48 eq.). For both cerium doped BiO-NCs, the Cotton effect signal of the BiO-NCs at 280 nm (**C-3:Ce**) and 277 nm (**C-4:Ce**) disappeared completely after adding the respective D-amino acid in an equimolar amount; thus no preference in chiral ligand binding was observed. Adding Boc-D-amino acids in excess to the BiO-NC solutions leads to a change of sign of the Cotton effect signal at ≈280 nm (Fig. S21†) and therefore a change in the chirality of the doped BiO-NCs. The CD-signal maximum of the cluster **C-3:Ce** (+48 eq. Boc-D-phenylalanine) at 286 nm is slightly shifted compared to the initial position at 282 nm. In contrast to **C-3:Ce**, the CD-signal maximum of **C-4:Ce** (+48 eq. Boc-D-alanine) at 277 nm (**C-4:Ce**) matches well

with the initial signal. *In situ* stability studies on cluster **C-4** at ambient and elevated temperature (*cf.* Fig. S22b and c†) do not show racemization over a period of 150 min. In conclusion, the accessibility of chiral cerium doped BiO-NCs was confirmed using different enantiomers of the respective ligand.

Nevertheless, cerium doping, as well as its oxidation state, is of inherent interest with regard to optical properties and will be discussed in the following in more detail. The transition between two stable oxidation states Ce(III/IV) often leads to the occurrence of mixed valence cerium oxido nanoclusters.[11,44,59,60] Studies demonstrated the sensitivity of the cerium oxidation state in mono and hexanuclear cerium complexes to the applied reaction conditions (pH), stabilizing ligand type, usage of additives or the kind of solvent.[44,45] For the previously published nitrate nanocluster **C-1:Ce**, the cerium oxidation state was found to be Ce(IV) based on the results obtained from XP- and UV–vis spectroscopy in the solid state.[36] However, ESI-MS revealed only species containing Ce(III) in the gas phase for all cerium doped clusters, which is explained for **C-1:Ce** by the reduction from Ce(IV) to Ce(III) caused by the loss of a nitrate radical. Such a reduction is not reported in the case of smaller homometallic cerium oxido nanoclusters coordinated by organic ligands such as acetylacetonate, for which fragments with both Ce(IV) and Ce(III) were identified in the mass spectra.[44,60] In the case of the carboxylate-functionalized BiO-NCs (**C-2:Ce–C-4:Ce**) reported here, the ESI MS results exclusively show the oxidation state Ce(III). XP spectroscopy was carried out to provide more detailed information about the oxidation state of cerium for Ce doped BiO-NCs. A representative survey spectrum of compound **C-4:Ce** as well as the high resolution spectra of N 1s, C 1s and O 1s core levels of BiO-NCs **C-1:Ce**, **C-2:Ce**, **C-3:Ce** and **C-4:Ce** are shown in the ESI (*cf.* Fig. S23†). XPS survey spectra confirmed the presence of the elements Bi, Ce, C, N, and O in all BiO-NCs. Sulfur cannot be detected in these samples due to the small photoemission cross section and overlap with the intense Bi 4f core level. As expected, the N 1s signal from nitrate observed at ≈407 eV in **C-1:Ce** is absent in the spectra of **C-2:Ce**, **C-3:Ce**, and **C-4:Ce** confirming the complete ligand exchange with the carboxylates. The BiO-NCs **C-3:Ce** and **C-4:Ce** show a signal at ≈400 eV arising from the amide group in the Boc-protected amino acid anion ligands. The respective high-resolution spectra of the Ce 3d core level are shown in Fig. 4. The Ce 3d signal is known to show distinct multiplet structures for different oxidation states due to final state effects.[61] The spin–orbit split duplet $v'''-u'''$, located at ≈898 eV and ≈917 eV, respectively, is characteristic of the Ce(IV) oxidation state. A peak deconvolution of the total Ce 3d core level signal can be used to quantify potential mixed valence states.[61] For homometallic cerium oxido nanoclusters and ceria, this fitting procedure is well established.[11,62,63] We calibrated our fitting procedure (*e.g.* peak separation and intensity, and full-width at half maximum) using both internal reference samples[36] and spectra available in the literature.[61] For the previously published cerium doped nitrate coordinated BiO-NC based on the presence of the single peak at around
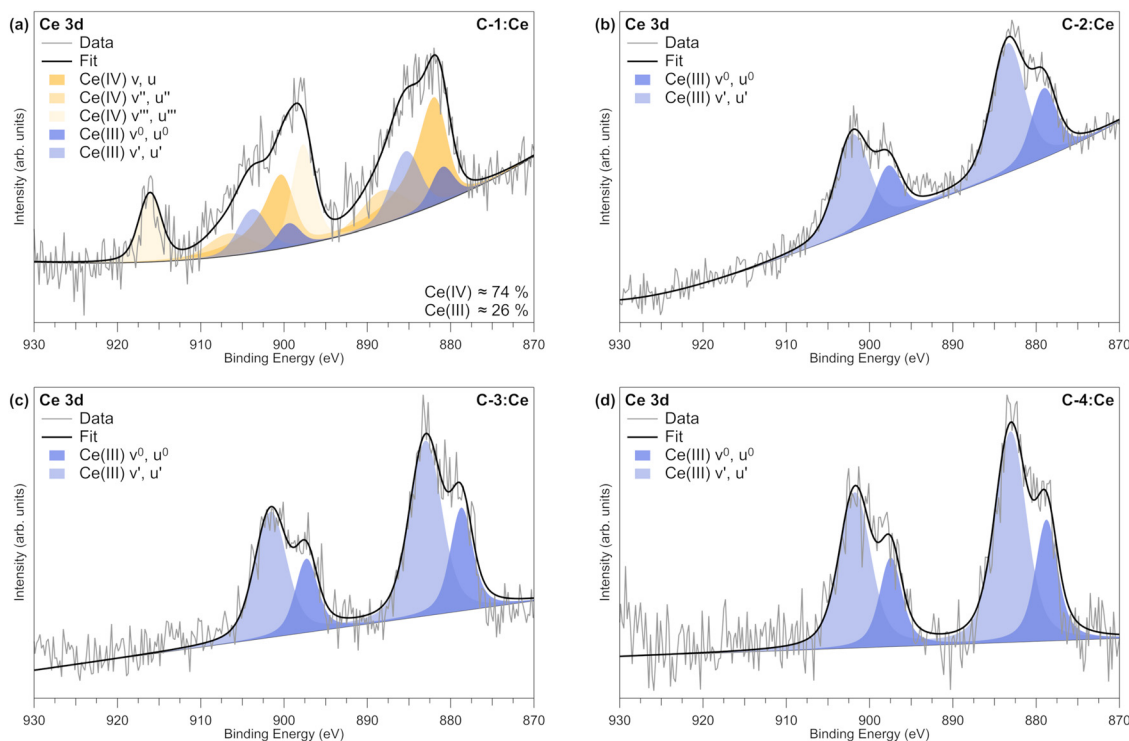
Fig. 4 XPS high-resolution spectra of cerium in the cerium doped BiO-NCs (a) **C-1:Ce**, (b) **C-2:Ce**, (c) **C-3:Ce** and (d) **C-4:Ce**. Two spin−orbit split peaks *v* and *u* correspond to each (final) state contributing to the spectra. Slight shifts in binding energy between different measurements are due to charging effects.

917 eV (Ce(IV) *v‴*) and the good agreement of a fit using only the Ce(IV) features *v*, *v″* and *v‴*, the data are decisive for the assignment to a Ce(IV) compound. However, the spectra for the as-synthesized compound **C-1:Ce** (Fig. 4a) using the modified synthesis protocol showed slightly different results and indicated a mixed-valence cerium doping of approximately Ce(IV) ≈74% and Ce(III) ≈26%. This ratio was obtained by fitting the spectra while constraining the intensity ratios and peak widths from the different Ce(IV) features *v*, *v″*, and *v‴*. The remaining peak area can be fitted well with the additional amount of Ce(III), using *v⁰*, *u⁰* and *v′*, *u′*.[11,61,62] The spectra of **C-2:Ce**, **C-3:Ce** and **C-4:Ce** show a distinctly different shape compared to **C-1:Ce**, as in all three spectra, the characteristic peak for Ce(IV) species at ≈917 eV is not detected. When the observed signals are fitted under the consideration of the intensity ratios of the *v⁰* and *v′* states in a Ce(III) compound, a good agreement is obtained. Thus, we conclude that under XPS conditions the NCs **C-2:Ce**, **C-3:Ce**, and **C-4:Ce** contain only Ce(III), whereas nitrate coordinated **C-1:Ce** consists of both Ce(III) and Ce(IV). We assume that the photoreduction of Ce(IV) complexes under oxidation of the solvent or the ligands took place upon modification of the nitrate **C-1:Ce** into the carboxylates.[64–66]

The presence of Ce(III) in all doped BiO-NCs was proven using continuous wave EPR spectroscopy at 10 K (*cf.* Fig. S24†). The obtained EPR signal clearly shows the presence of Ce(III) as an S = 1/2 species and matches well with the EPR spectra of the respective cerium oxido nanoclusters.[11,67–70]

Cerium compounds typically appear yellow as a result of mixed valency, defective structures, MLCT from Ce(III) or LMCT to Ce(IV) leading to a red-shifted and broader absorption in the visible light region.[59,64,71] Similarly, the cerium doped BiO-NCs (**C-1:Ce–C-4:Ce**) synthesized in this study are obtained as orange-yellow crystalline materials, while the undoped clusters are colorless. The red-shifted absorption of the previously reported nitrate coordinated BiO-NC has previously been attributed to an LMCT of oxygen to cerium(IV).[36] The nitrate cluster **C-1:Ce** reported here appears mixed-valent, while in the carboxylate substituted BiO-NCs (**C-2:Ce–C-4:Ce**), only Ce(III) is present. The influence of cerium on the resulting UV-Vis spectra in diffuse reflectance for the doped BiO-NCs was therefore investigated in comparison with the undoped BiO-NCs (Fig. 5 and Table S12†). Note that all BiO-NCs were ground for better comparability, since effects such as crystal size, roughness or thickness of the sample have a strong influence on the resulting spectra (*cf.* Fig. S25a†). Based on the corresponding UV-vis spectra, the absorption edges of compounds **C-1**, **C-2**, **C-3** and **C-4** with values between 340 nm and 353 nm (3.5 eV–3.6 eV) are in the UV region, whereas those of the cerium doped nanoclusters **C-1:Ce**, **C-2:Ce**, **C-3:Ce** and **C-4:Ce** are red-shifted by 100 nm–130 nm to the visible region in between 445 nm and 478 nm (2.6 eV–2.8 eV; *cf.* Table S12†). It is noteworthy that the spectra of the cerium doped clusters agree well with those of the undoped clusters in the range between 325 nm and 250 nm, showing strong absorption with a
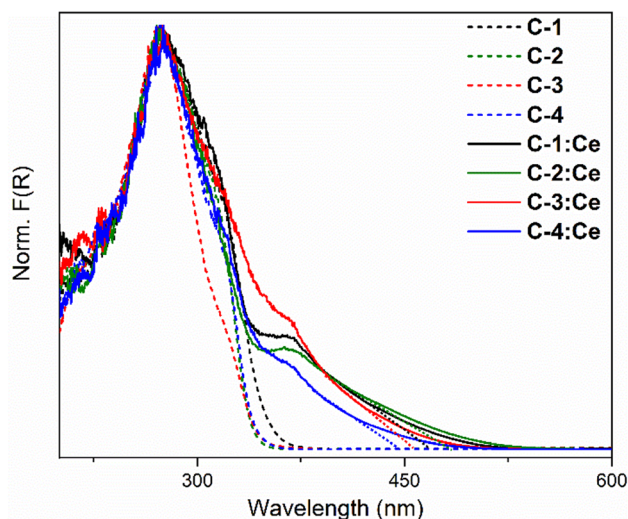
Fig. 5 UV–vis spectra in diffuse reflection of BiO-NCs **C-1** (black dotted), **C-1:Ce** (black), **C-2** (green dotted), **C-2:Ce** (green), **C-3** (red dotted), **C-3:Ce** (red), **C-4** (blue dotted) and **C-4:Ce** (blue).

maximum at 270 nm–275 nm, which is assigned to the absorption of the $\{Bi_{38}O_{45}\}$ core, but they differ in an additional band at about 365 nm, which is present in all cerium doped clusters. Thus, cerium doping ($\approx 1 \ \omega\%$) strongly influences the absorption, leading to a clear color change and a shift of the optical energy gap to the visible region (2.6 eV–2.8 eV). The additional absorption in the cerium doped clusters differs slightly in intensity, onset and edge, but there is no correlation with the cerium content (**C-4:Ce** highest, **C-2:Ce** lowest) or cerium oxidation state (**C-1:Ce** similar to **C-2:Ce–C-4:Ce**). Furthermore, the absorption band is not significantly influenced by the coordinated ligands to the BiO-NCs, suggesting that MLCT effects occur between cerium(III) and oxygen within the core and not between cerium and carboxylates, further supporting the location of cerium in the inner region of the $\{Bi_{38-x}Ce_xO_{45}\}$ cluster motif. It should be noted that cerium as the absorption center (*e.g.* in $Ce(NO_3)_3 \cdot 5H_2O$ *cf*. Fig. S25b†) absorbs light in the UV-region only.

The PL emission spectra (*cf*. Fig. S26†) of the cerium doped clusters **C-2:Ce–C-4:Ce** were measured in a saturated solution of NCs in ethanol, whereas **C-1:Ce** had to be dissolved in DMSO. All BiO-NCs show similar broad emission bands between 450 nm–650 nm under excitation with 386 nm. In accordance with the results of our study, broad signals in a similar range are reported for both Ce(III) and Bi(III) photoluminescence in the literature, wherefore a clear assignment is not possible.[72–75]

In summary, the presence of Ce(III) in all cerium doped BiO-NCs was proven by XP and EPR spectroscopy. Ce(IV) was determined only for the nitrate **C-1:Ce** based on XPS investigations. However, the high Ce(IV) amount and mixed valency in **C-1:Ce** do not affect the EPR, PL and UV–vis spectroscopic results significantly compared to those of Ce(III) containing carboxylate modified cerium doped clusters.

An important feature of atomically precise BiO-NCs is their stability and molecular integrity in the solid phase, gas phase and solution. While the nitrate functionalized BiO-NCs **C-1** and **C-1:Ce** are only soluble in DMSO, the carboxylate clusters **C-2(:Ce)–C4(:Ce)** are soluble in several polar organic solvents such as ethanol, acetonitrile or 1-octanol, making them interesting for film processing. In addition to NMR spectroscopy, particle size distribution (PSD) measurements based on dynamic light scattering (DLS) experiments were used to confirm the integrity of the BiO-NCs in solution and further to determine their hydrodynamic diameters (Fig. S27–S33†). The BiO-NCs show a narrow size distribution that matches well with the cluster size determined from PXRD. The hydrodynamic diameters of **C-1** and **C-1:Ce** in DMSO were determined as 1.1 nm and 1.3 nm, respectively. The diameters of the carboxylate substituted BiO-NCs were measured in ethanol and 1-octanol, respectively. BiO-NCs **C-2** and **C-2:Ce** exhibit diameters between 2.4 nm and 2.7 nm in ethanol and octanol, respectively. The measurements demonstrate the increased size of the NCs as a result of the larger coordinating organic ligand shell and stronger interactions with the solvents. The diameter of **C-3** of ≈ 2.7 nm is almost the same in both solvents, whereas the diameter of compound **C-3:Ce** ranges from a slightly smaller value of 2.3 nm in ethanol, to a similar value of 2.8 nm in 1-octanol. BiO-NCs **C-4** and **C-4:Ce** show somewhat larger differences in the hydrodynamic diameters, with **C-4:Ce** showing smaller values of 2.2 nm in ethanol and 2.6 nm in 1-octanol, whereas **C-4** shows diameters of 2.5 nm and 3.1 nm, respectively.

In the previous sections, the successful synthesis and characterization of organically modified BiO-NCs was demonstrated. The BiO-NCs **C-3** and **C-3:Ce** show high solubility in ethanol, are stable in solution and contain a high cerium content. As promising candidates for deposition experiments, these nanoclusters were chosen for an investigation of their self-assembly on Au(111) and highly ordered pyrolytic graphite HOPG(0001) using STM in order to gain a deeper understanding of their interaction with surfaces. The deposition of metal oxido nanoclusters on Au(111) and their investigation using STM/STS was reported for MO-NCs functionalized with sulfur-containing ligands to enable binding with gold,[76–78] while it was thoroughly reported for POMs using diverse ligands.[79–85] The BiO-NCs **C-3** and **C-3:Ce** bind well to the Au(111) surface *via* van der Waals forces without the need for sulfur-containing anchor groups. The different coverages of **C-3** and **C-3:Ce** on Au(111) and HOPG(0001) substrates in the STM experiments were controlled by using sample solutions with two different concentrations, 0.4 mM (Fig. 6a, c and e) to 1.2 mM (Fig. 6b, d and f).

Starting with their adsorption on the Au(111) surfaces, the STM images show randomly adsorbed **C-3** NCs. The density of BiO-NCs amounts to 0.1 molecules per nm^2 (panel a) and 0.14 molecules per nm^2 (panel b) for the 0.4 mM and 1.2 mM solution, respectively. Individual nanoclusters can be resolved as bright spots and their diameters of about 2.2 nm fit well with the results obtained by DLS (2 nm–2.8 nm) and PXRD
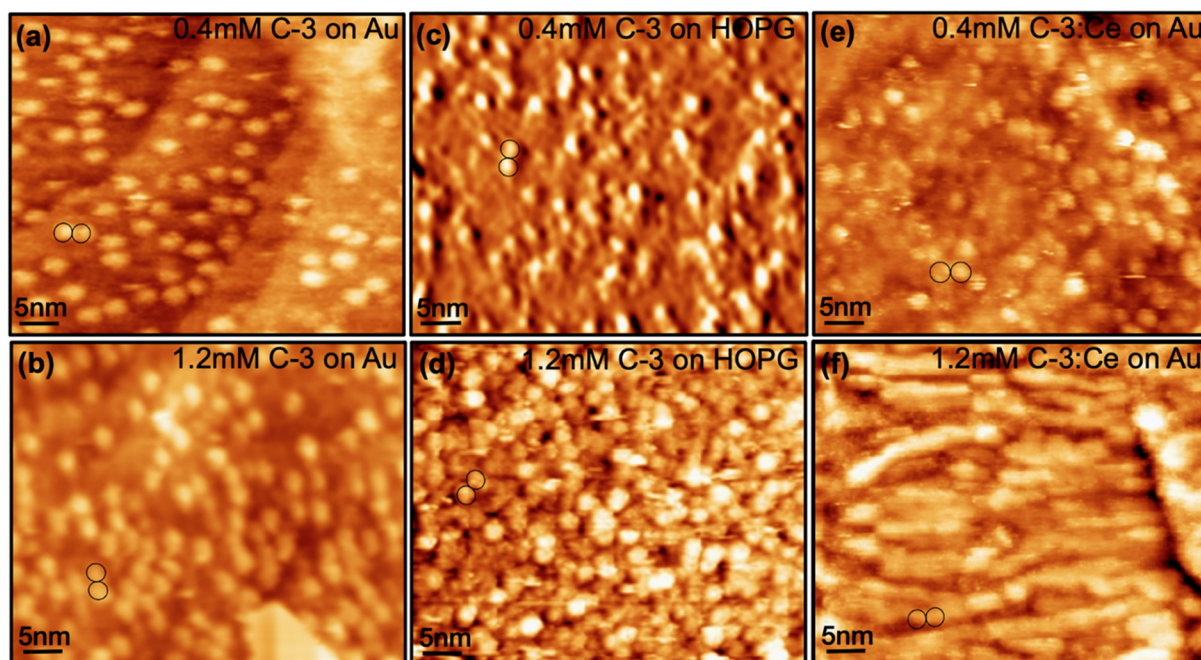
Fig. 6 **C-3** and **C-3:Ce** on Au(111) and HOPG(0001) surfaces controlled by concentration after 5 minutes of deposition (a and b) STM images of the **C-3** nanocluster on Au(111) surfaces for low (0.4 mM) and high (1.2 mM) concentrations. (c and d) STM images of **C-3** on HOPG surfaces for low and high concentrations. (e and f) STM images of cerium doped nanocluster **C-3:Ce** on Au(111) surfaces for low and high concentrations. For the images, tunneling conditions of +1.0 V, 1.5 nA were used.

(≈2 nm) experiments. However, **C-3** molecules often tend to form pairs or even chains, seen for both coverages. The Au (111) surface exhibits a so-called herringbone reconstruction showing periodicities of 2.8 nm and 3.8 nm. Since we did not find any of these length scales, we conclude that the details of the Au-terrace structure are not decisive for the adsorption behavior. A similar trend was also observed on plasma-cleaned HOPG(0001) substrates as shown in Fig. 6c and d for the low (0.4 mM) and high concentration (1.2 mM), respectively. It is important to note that the coupling of **C-3** NCs to perfect sites on the HOPG terraces is very weak, so that preferential adsorption at step edges was found. Therefore, in order to increase the adsorption rate on the terraces, defects were introduced by mild plasma cleaning prior to adsorption from the solution. Moreover, we also studied the adsorption behavior of **C-3:Ce** NCs. The structures on Au(111) and HOPG(0001) were formed in the same manner using the same concentrations of the solutions. Compared to **C-3**, the adsorption of **C-3:Ce** on Au (111) shows a similar structure for the 0.4 mM solution shown in Fig. 6e. However, a chain-like structure was obtained in the case of the higher concentrated solution (1.2 mM), as shown in Fig. 6f. This chain-like structure, which is apparently a consequence of an effective nanocluster–nanocluster interaction, will be discussed in more detail below.

We further utilized STS to investigate the electronic structure of **C-3** and **C-3:Ce** nanoclusters adsorbed on HOPG(0001) and Au(111) surfaces. From the dI/dV spectra, which are to a first order proportional to the density of states, we can determine the energetic positions of the highest and lowest occu-

pied molecular orbitals (HOMO and LUMO) of the nanoclusters with respect to the Fermi levels of the supports. As shown in Fig. 7, the electronic energy gap for **C-3** on Au and HOPG is around 3.5 eV, which is in good agreement with the optical energy gap of 3.6 eV as determined from UV–vis data (Table S12†). The LUMO (HOMO) states are well above (below) the Fermi energy; thus the charge state of BiO-NCs upon adsorption is not considerably changed. This confirms that compound **C-3** is (electronically) intact upon adsorption, showing a weak interaction with the substrate. However, the shift seems to be not simply induced by the difference in the work functions, since this would result in an opposite trend. The electronic energy gap of **C-3:Ce** is considerably smaller than in **C-3**. Apparently, by doping the nanocluster with Ce, new in-gap states are formed reducing the gap to 2.6 eV. This reduction of the electronic energy gap compared to **C-3** agrees well with the optical energy gap of 2.7 eV as estimated from the UV–vis data (Table S12†). Apart from the additional in-gap states in **C-3:Ce**, the STS curves of **C-3** and **C-3:Ce** show a very similar curve profile, consistent with their description as a mixture of undoped (35%) and doped (65%) BiO-NCs. Furthermore, the **C-3** and **C-3:Ce** spectra on Au are not shifted against each other, *i.e.* any charge transfer between the NCs and the surface must be rather small. As discussed above, the nanocluster–substrate interaction is weak. In the following, we would like to highlight the nanoluster–nanocluster interaction and the resulting self-assembly which were seen particularly in the high coverage regime, *e.g.* in Fig. 6f. In Fig. 8d, chain-like arrangements of **C-3:Ce** are observed at low concentration and
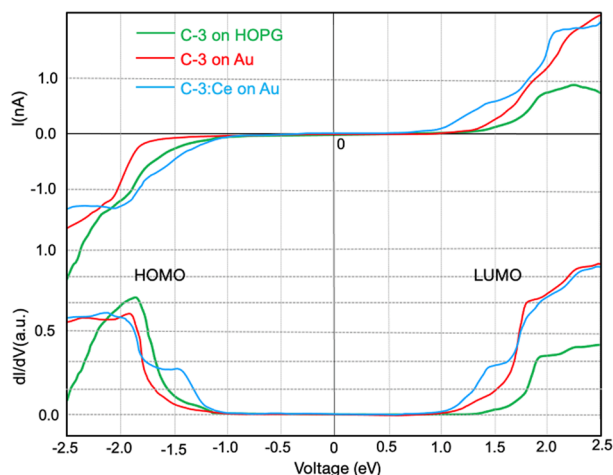
Fig. 7 STS spectra of **C-3** on Au(111) (red curve), **C-3** on HOPG(0001) (green curve) surfaces, and cluster **C-3:Ce** on Au(111) (blue curve). Set point for the STS measurements was +1.0 eV, 1.5 nA.
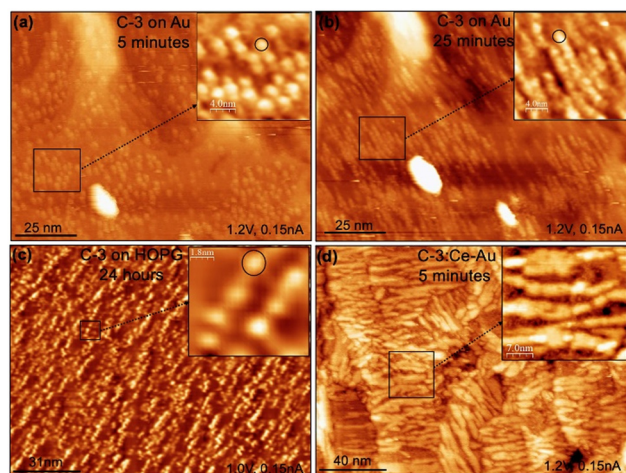

Fig. 8 STM images of the **C-3** nanocluster on the Au(111) surface from high concentration solution after 5 minutes (a) and 25 minutes (b); chain-like assembled structure of **C-3** on the defective HOPG surface from high concentration solution after one day (c), and of **C-3:Ce** doped on the Au surface observed from high concentration solution after 5 minutes (d).

short adsorption time, suggesting that the interactions between the **C-3:Ce** nanoclusters must be large. However, undoped **C-3** chains can also be formed, *i.e.* by increasing the time of adsorption of the BiO-NCs or by increasing the concentration on the surface. Fig. 8a and b illustrate the transition from single nanoclusters towards chains (consisting of around ten **C-3** BiO-NCs) by increasing the adsorption time by a factor of five. Moreover, using plasma-treated HOPG templates, similar chain structures can be formed on the terraces of HOPG as shown in Fig. 8c. As a result of doping with Ce, a slightly larger intrinsic dipole moment is assumed for **C-3:Ce** NCs compared to **C-3**, favoring the chain-like alignment. We explain this increased intrinsic dipole with substitution of the

larger bismuth(III) cation by the smaller cerium cation with lower electronegativity ($r_{Bi_{3+}}$ 117 pm *vs.* $r_{Ce_{3+}}$ 114.3 pm effective ionic radius for coordination number 8, respectively; Pauling electronegativity Bi 1.9 *vs.* Ce 1.4) resulting in symmetry breaking of the nanoclusters which should result in their polarization.[86,87] Note that a dipole-induced influence on physical properties was recently reported for heterometallic polyoxotitanium clusters of the type $[Ti_xO_y(OR)_zM_nX_m]$ (M = metal dopant ion, X = inorganic anion).[42] In addition, there are several reports on chain phase formation driven by competing short-range attractive and long-range repulsive interactions, where anisotropic dipole–dipole interactions are present.[88–95] To rationalize the chain formations displayed in the present work, we also use the charge transfer model due to substrate induced charge effect as the nanoclusters are brought close to the substrate surface upon adsorption. Thereby, the charge transfer between the surface and BiO-NCs seems to be small. However, the dispersion forces between the substrate surface and the large NC shell are not negligible, leading to an increase in the local dipole moments and, concomitantly, indirect triggering of the formation of BiO-NC-chains, if the density of nanoclusters is high enough. This is pronounced in **C-3:Ce** NCs, where cerium doping is assumed to induce an intrinsic dipole moment.

Conclusions

Atomically precise metal oxido nanoclusters might serve as soluble model compounds for nanoparticles and provide a link between a nanoparticulate and molecular picture. This might help provide a deeper understanding of the effects of doping and surface modification of nanoparticles. In particular, bismuth oxido nanoclusters have been demonstrated to be models for bismuth oxide nanoparticles. Herein, we extend this concept with results on doping and ligand shell functionalization of these nanoclusters. Starting from the BiO-NC $[Bi_{38}O_{45}(NO_3)_{24}(dmso)_{28}]$:Ce (**C-1:Ce**), ligand modified BiO-NCs are obtained by reaction with carboxylates to give $[Bi_{38}O_{45}(L)_{24}]$:Ce, L = $^-$OMc (**2**), Boc-L-Phe–O$^-$ (**3**) and Boc-L-Ala–O$^-$ (**4**). Thus, doped and undoped soluble atomically precise nanoclusters with a size of ≈2 nm with a chiral ligand shell become available. The obtained doping content of ≈1 ω% affects the molecular structure of BiO-NCs to only a minor extent but is significant with regard to their physical properties. The BiO-NC core becomes paramagnetic due to the presence of Ce(III) as demonstrated by EPR, which however does not affect the NC ^{1}H NMR spectrum in solution. The optical and electronic energy gap can be significantly lowered upon doping from the UV to the visible region (3.6 eV–3.5 eV *vs.* 2.6 eV–2.8 eV). The STM studies reveal a supramolecular self-assembly in chain-like arrangements of the nanoclusters which suggest the presence of some intrinsic dipole moment in line with SC XRD analysis showing anisotropic occupational disorder of the Bi/Ce positions. With regard to the molecular structure, it is important to note that unlike in other heterome-

tallic metal oxido clusters, the metal cation positions of the host element bismuth are randomly substituted by cerium with preference to the inner core positions. ESI MS studies demonstrate that up to three bismuth atoms are substituted by cerium in the nanoclusters, but mono-substitution dominates. Consequently, and in line with the small amount of doping, the crystalline material consists of doped and undoped nanoclusters. A comparable situation is expected for doping in bulk metal oxides, showing anisotropic nanophase domains. Another intriguing feature observed is the oxidation state change of cerium in $[Bi_{38}O_{45}(L)_{24}]$:Ce, when substituting the nitrate ligand by organic carboxylates under ambient conditions. The nitrate substituted BiO-NC is of mixed valent nature showing Ce(III) and Ce(IV), whereas the organically modified nanoclusters are found to solely contain Ce(III) based on XPS and EPR studies. Thus, surface modification by treatment under ambient conditions either with nitrate or organic carboxylates alters the electronic situation of cerium containing metal oxide nanoclusters significantly. Since most of the cerium atoms are placed in an inner core position, the ligand surface effect on electron transfer is of long range order. With regard to applications in (opto)spintronics using hyperpolarization, our results demonstrate that (i) monolayers of chirally modified Ce doped BiO-NCs can be prepared by solution-based processes; (ii) their optical and electronic energy gaps can be modulated by doping without significant structural changes; (iii) ligand substitution from a nitrate to carboxylate induces electron transfer in the inner core of the cluster without a significant change in the metal oxido core structure; (iv) STS reveals electron transport through the cluster; and (v) chiral BiO-NCs show a robust and invertible CD signal. To what extent the electron transport across the chiral BiO-NCs will show a CISS (chirality induced spin selectivity) effect will be studied in the future by STM and STS, both of which have been demonstrated to be valuable analytical tools in this context.[96] The physical properties of monolayers of the here reported BiO-NCs can be modified by introducing other metal cations into the bismuth oxido matrix and by variation of the ligand shell, which is currently under investigation.

Author contributions

R. T.: conceptualization, investigation, formal analysis, visualization, writing – original draft, and review & editing; T. N. H. N.: STM and STS measurements and analysis, writing – original draft, review & editing, and visualization; M. W.: ESI-MS measurements and analysis, and writing – review & editing; T. R.: single-crystal measurements and analysis and writing – review & editing; F. G. XPS measurements and analysis, visualization, and writing – review & editing; A. D.: EPR measurements and analysis, and writing – review & editing; A. P.: supervision, funding acquisition, resources, and writing – review & editing; T. S.: supervision, resources, and writing – review & editing; C. T.: supervision, funding acquisition, resources, and writing – review & editing; and M. M.: supervi-

sion, conceptualization, resources, writing – review & editing, and funding acquisition. All authors have given approval to the final version of the manuscript.

Conflicts of interest

There are no conflicts to declare.

Data availability

The data supporting our findings in this article have been included as part of the ESI.† CCDC 2386322 (**C-2**) and 2386323 (**C-2:Ce**)† contain the supplementary crystallographic data for this paper.

Acknowledgements

References

1 R. P. Feynman, There's Plenty of Room at the Bottom, *Eng. Sci.*, 1960, **23**, 22–36.

2 X. Fu, J. Cai, X. Zhang, W.-D. Li, H. Ge and Y. Hu, Top-down fabrication of shape-controlled, monodisperse nanoparticles for biomedical applications, *Adv. Drug Delivery Rev.*, 2018, **132**, 169–187.

3 J. Park, J. Joo, S. G. Kwon, Y. Jang and T. Hyeon, Synthesis of Monodisperse Spherical Nanocrystals, *Angew. Chem., Int. Ed.*, 2007, **46**, 4630–4660.

4 M. Muzzio, J. Li, Z. Yin, I. M. Delahunty, J. Xie and S. Sun, Monodisperse nanoparticles for catalysis and nanomedicine, *Nanoscale*, 2019, **11**, 18946–18967.

5 X. Kang, Y. Li, M. Zhu and R. Jin, Atomically precise alloy nanoclusters: syntheses, structures, and properties, *Chem. Soc. Rev.*, 2020, **49**, 6443–6514.

6 X. Kang and M. Zhu, Transformation of Atomically Precise Nanoclusters by Ligand-Exchange, *Chem. Mater.*, 2019, **31**, 9939–9969.

7 Y. Du, H. Sheng, D. Astruc and M. Zhu, Atomically Precise Noble Metal Nanoclusters as Efficient Catalysts: A Bridge

between Structure and Properties, *Chem. Rev.*, 2020, **120**, 526–622.

8   J. Zhang, P. Feng, X. Bu and T. Wu, Atomically precise metal chalcogenide supertetrahedral clusters: frameworks to molecules, and structure to function, *Natl. Sci. Rev.*, 2021, **9**, nwab076.

9   S. Dehnen and J. Corrigan, *Clusters-contemporary insight in structure and bonding*, Springer International Publishing, Cham, 2017.

10 I. L. Malaestean, A. Ellern, S. Baca and P. Kögerler, Cerium oxide nanoclusters: commensurate with concepts of polyoxometalate chemistry?, *Chem. Commun.*, 2012, **48**, 1499–1501.

11 K. J. Mitchell, K. A. Abboud and G. Christou, Atomically-precise colloidal nanoparticles of cerium dioxide, *Nat. Commun.*, 2017, **8**, 1445–1452.

12 M. Schlesinger, M. Weber, S. Schulze, M. Hietschold and M. Mehring, Metastable β-Bi_2O_3 Nanoparticles with Potential for Photocatalytic Water Purification Using Visible Light Irradiation, *ChemistryOpen*, 2013, **2**, 146–155.

13 C. Falaise, C. Volkringer, J.-F. Vigier, A. Beaurain, P. Roussel, P. Rabu and T. Loiseau, Isolation of the Large {Actinide}$_{38}$ Poly-oxo Cluster with Uranium, *J. Am. Chem. Soc.*, 2013, **135**, 15678–15681.

14 L. Soderholm, P. M. Almond, S. Skanthakumar, R. E. Wilson and P. C. Burns, The Structure of the Plutonium Oxide Nanocluster $[Pu_{38}O_{56}Cl_{54}(H_2O)_8]^{14-}$, *Angew. Chem., Int. Ed.*, 2008, **47**, 298–302.

15 R. E. Wilson, S. Skanthakumar and L. Soderholm, Separation of Plutonium Oxide Nanoparticles and Colloids, *Angew. Chem., Int. Ed.*, 2011, **50**, 11234–11237.

16 K. H. Whitmire and K. Wall, The oxido clusters of bismuth, *Coord. Chem. Rev.*, 2023, **488**, 215072.

17 M. Mehring, From molecules to bismuth oxide-based materials: Potential homo- and heterometallic precursors and model compounds, *Coord. Chem. Rev.*, 2007, **251**, 974–1006.

18 M. Mehring and S. Dehnen, in *Clusters – Contemporary Insight in Structure and Bonding*, Springer International Publishing, Cham, 2017, vol. 174, pp. 201–268.

19 M.-Y. Gao, F. Wang, Z.-G. Gu, D.-X. Zhang, L. Zhang and J. Zhang, Fullerene-like Polyoxotitanium Cage with High Solution Stability, *J. Am. Chem. Soc.*, 2016, **138**, 2556–2559.

20 J. Hou, J. Hu, Q. Sun, G. Zhang, C.-H. Tung and Y. Wang, A Post-Functionalizable Iso-Polyoxotitanate Cage Cluster, *Inorg. Chem.*, 2016, **55**, 7075–7078.

21 K. Wu, L. Shao, X. Jiang, M. Shui, R. Ma, M. Lao, X. Lin, D. Wang, N. Long, Y. Ren and J. Shu, Facile preparation of $[Bi6O4](OH)4(NO3)6\cdot4H_2O$, $[Bi6O4](OH)4(NO3)6\cdotH_2O$ and $[Bi6O4](OH)4(NO3)6\cdotH_2O/C$ as novel high capacity anode materials for rechargeable lithium-ion batteries, *J. Power Sources*, 2014, **254**, 88–97.

22 L. Miersch, T. Rüffer and M. Mehring, Organic–inorganic hybrid materials starting from the novel nanoscaled bismuth oxido methacrylate cluster $[Bi_{38}O_{45}(OMc)_{24}(DMSO)_9]\cdot2DMSO\cdot7H_2O$, *Chem. Commun.*, 2011, **47**, 6353–6355.

23 M. Schlesinger, M. Weber, T. Rüffer, H. Lang and M. Mehring, Nanoscaled Bismuth Oxido Clusters: Probing Factors of Structure Formation and Photocatalytic Activity, *Eur. J. Inorg. Chem.*, 2014, **2014**, 302–309.

24 K. Zhou, G. Ding, C. Zhang, Z. Lv, S. Luo, Y. Zhou, L. Zhou, X. Chen, H. Li and S.-T. Han, A solution processed metal–oxo cluster for rewritable resistive memory devices, *J. Mater. Chem. C*, 2019, **7**, 843–852.

25 A. Morgenstern, R. Thomas, A. Sharma, M. Weber, O. Selyshchev, I. Milekhin, D. Dentel, S. Gemming, C. Tegenkamp, D. R. T. Zahn, M. Mehring and G. Salvan, Deposition of Nanosized Amino Acid Functionalized Bismuth Oxido Clusters on Gold Surfaces, *Nanomaterials*, 2022, **12**, 1815–1832.

26 D. Mansfeld, L. Miersch, T. Rüffer, D. Schaarschmidt, H. Lang, T. Böhle, R. W. Troff, C. A. Schalley, J. Müller and M. Mehring, From {$Bi_{22}O_{26}$} to Chiral Ligand–Protected {$Bi_{38}O_{45}$}–Based Bismuth Oxido Clusters, *Chem. – Eur. J.*, 2011, **17**, 14805–14810.

27 L. Miersch, T. Rüffer, M. Schlesinger, H. Lang and M. Mehring, Hydrolysis Studies on Bismuth Nitrate: Synthesis and Crystallization of Four Novel Polynuclear Basic Bismuth Nitrates, *Inorg. Chem.*, 2012, **51**, 9376–9384.

28 D. Szczerba, D. Tan, J.-L. Do, H. M. Titi, S. Mouhtadi, D. Chaumont, M. C. Marco de Lucas, N. Geoffroy, M. Meyer, Y. Rousselin, J. M. Hudspeth, V. Schwanen, P. Spoerk-Erdely, A.-C. Dippel, O. Ivashko, O. Gutowski, P. Glaevecke, V. Bazhenov, M. Arhangelskis, I. Halasz, T. Friščić and S. A. J. Kimber, Real-Time Observation of "Soft" Magic-Size Clusters during Hydrolysis of the Model Metallodrug Bismuth Disalicylate, *J. Am. Chem. Soc.*, 2021, **143**, 16332–16336.

29 L. Wrobel, T. Rüffer, M. Korb, H. Krautscheid, J. Meyer, P. C. Andrews, H. Lang and M. Mehring, Homo- and Heteroleptic Coordination Polymers and Oxido Clusters of Bismuth(III) Vinylsulfonates, *Chem. – Eur. J.*, 2018, **24**, 16630–16644.

30 V. André, A. Hardeman, I. Halasz, R. S. Stein, G. J. Jackson, D. G. Reid, M. J. Duer, C. Curfs, M. T. Duarte and T. Friščić, Mechanosynthesis of the metallodrug bismuth subsalicylate from Bi_2O_3 and structure of bismuth salicylate without auxiliary organic ligands, *Angew. Chem.*, 2011, **123**, 8004–8007.

31 V. Chandrasekhar, R. K. Metre and D. Sahoo, Bi_{38} Oxocarboxylate Cages are Keplerates – Synthesis and Structural Characterization of Two Bi_{38} Oxocarboxylate Cages, *Eur. J. Inorg. Chem.*, 2014, **2014**, 164–171.

32 P. C. Andrews, M. Busse, P. C. Junk, C. M. Forsyth and R. Peiris, Sulfonato-encapsulated bismuth(III) oxido-clusters from Bi_2O_3 in water under mild conditions, *Chem. Commun.*, 2012, **48**, 7583–7585.

33 L. Miersch, T. Rüffer, D. Schaarschmidt, H. Lang, R. W. Troff, C. A. Schalley and M. Mehring, Synthesis and

Characterization of Polynuclear Oxidobismuth Sulfonates, *Eur. J. Inorg. Chem.*, 2013, **2013**, 1427–1433.

34 L. Wrobel, T. Rüffer, M. Korb, H. Lang and M. Mehring, Bismuth(III) Anthranilates – Synthesis and Characterization of a Coordination Polymer and a Polynuclear Oxido Cluster, *Eur. J. Inorg. Chem.*, 2017, **2017**, 1032–1040.

35 Q.-R. Ding, Y. Yu, C. Cao, J. Zhang and L. Zhang, Stepwise assembly and reversible structural transformation of ligated titanium coated bismuth-oxo cores: shell morphology engineering for enhanced chemical fixation of CO_2, *Chem. Sci.*, 2022, **13**, 3395–3401.

36 M. Weber, T. Rüffer, F. Speck, F. Göhler, D. P. Weimann, C. A. Schalley, T. Seyller, H. Lang and M. Mehring, From a Cerium-Doped Polynuclear Bismuth Oxido Cluster to β-Bi_2O_3:Ce, *Inorg. Chem.*, 2020, **59**, 3353–3366.

37 A. Ghosh, O. F. Mohammed and O. M. Bakr, Atomic-Level Doping of Metal Clusters, *Acc. Chem. Res.*, 2018, **51**, 3094–3103.

38 J. Yang, R. Pang, D. Song and M.-B. Li, Tailoring silver nanoclusters via doping: advances and opportunities, *Nanoscale Adv.*, 2021, **3**, 2411–2422.

39 V. Yadav, A. Jana, S. Acharya, S. Malola, H. Nagar, A. Sharma, A. R. Kini, S. Antharjanam, J. Machacek, K. N. V. D. Adarsh, T. Base, H. Häkkinen and T. Pradeep, Site-specific substitution in atomically precise carboranethiol-protected nanoclusters and concomitant changes in electronic properties, *Nat. Commun.*, 2025, **16**, 1197.

40 P. Coppens, Y. Chen and E. Trzop, Crystallography and Properties of Polyoxotitanate Nanoclusters, *Chem. Rev.*, 2014, **114**, 9645–9661.

41 Y.-J. Liu, W.-H. Fang, L. Zhang and J. Zhang, Recent advances in heterometallic polyoxotitanium clusters, *Coord. Chem. Rev.*, 2020, **404**, 213099.

42 Y. Lv, J. Cheng, A. Steiner, L. Gan and D. S. Wright, Dipole-Induced Band-Gap Reduction in an Inorganic Cage, *Angew. Chem., Int. Ed.*, 2014, **53**, 1934–1938.

43 J. Wang, F. Gao, D. Wang, Y. Li, L. Linping, G. Zhang, G. Wang, C.-H. Tung and Y. Wang, Electronic State Modulation of a Single-Cu Site on a Bimetallically Doped Titanium-Oxo Cluster to Enhance CO_2 Storage, *Angew. Chem., Int. Ed.*, 2025, e202505584.

44 W.-D. Liu, L.-Q. Chen, Q.-H. Qiu, M.-Q. Qi, H. Xu, C.-L. Chen, L.-S. Long, L.-S. Zheng and X.-J. Kong, A mixed valence decanuclear cerium-oxo cluster $CeIII_4CeIV_6$ for efficient photocurrent response, *Inorg. Chem. Commun.*, 2024, **159**, 111763.

45 N. A. Piro, J. R. Robinson, P. J. Walsh and E. J. Schelter, The electrochemical behavior of cerium(III/IV) complexes: Thermodynamics, kinetics and applications in synthesis, *Coord. Chem. Rev.*, 2014, **260**, 21–36.

46 S. L. Estes, M. R. Antonio and L. Soderholm, Tetravalent Ce in the Nitrate-Decorated Hexanuclear Cluster $[Ce_6(\mu^3\text{-}O)_4(\mu^3\text{-}OH)_4]^{12+}$: A Structural End Point for Ceria Nanoparticles, *J. Phys. Chem. C*, 2016, **120**, 5810–5818.

47 K. Ackland and J. M. D. Coey, Room temperature magnetism in CeO_2—A review, *Phys. Rep.*, 2018, **746**, 1–39.

48 S. Kano, T. Tada and Y. Majima, Nanoparticle characterization based on STM and STS, *Chem. Soc. Rev.*, 2015, **44**, 970–987.

49 T. S. Basu, S. Diesch, R. Hayakawa, Y. Wakayama and E. Scheer, Single-charge transport through hybrid core–shell Au-ZnS quantum dots: a comprehensive analysis from a modified energy structure, *Nanoscale*, 2021, **13**, 4978–4984.

50 R. Jin, C. Zeng, M. Zhou and Y. Chen, Atomically precise colloidal metal nanoclusters and nanoparticles: fundamentals and opportunities, *Chem. Rev.*, 2016, **116**, 10346–10413.

51 T. Ohgi, H.-Y. Sheng, Z.-C. Dong and H. Nejoh, Observation of Au deposited self-assembled monolayers of octanethiol by scanning tunneling microscopy, *Surf. Sci.*, 1999, **442**, 277–282.

52 T. Ohgi, H.-Y. Sheng, Z.-C. Dong, H. Nejoh and D. Fujita, Charging effects in gold nanoclusters grown on octanedithiol layers, *Appl. Phys. Lett.*, 2001, **79**, 2453–2455.

53 P. Yang, I. Arfaoui, T. Cren, N. Goubet and M.-P. Pileni, Electronic properties probed by scanning tunneling spectroscopy: From isolated gold nanocrystal to well-defined supracrystals, *Phys. Rev. B: Condens. Matter Mater. Phys.*, 2012, **86**, 075409.

54 L. Miersch, M. Schlesinger, R. W. Troff, C. A. Schalley, T. Rüffer, H. Lang, D. Zahn and M. Mehring, Hydrolysis of a Basic Bismuth Nitrate—Formation and Stability of Novel Bismuth Oxido Clusters, *Chem. – Eur. J.*, 2011, **17**, 6985–6990.

55 M. Schlesinger, S. Schulze, M. Hietschold and M. Mehring, Metastable β-Bi_2O_3 nanoparticles with high photocatalytic activity from polynuclear bismuth oxido clusters, *Dalton Trans.*, 2013, **42**, 1047–1056.

56 A. S. Anker, T. L. Christiansen, M. Weber, M. Schmiele, E. Brok, E. T. S. Kjær, P. Juhás, R. Thomas, M. Mehring and K. M. Ø. Jensen, Structural Changes during the Growth of Atomically Precise Metal Oxido Nanoclusters from Combined Pair Distribution Function and Small-Angle X-ray Scattering Analysis, *Angew. Chem., Int. Ed.*, 2021, **60**, 20407–20416.

57 D. Sattler, M. Schlesinger, M. Mehring and C. A. Schalley, Mass Spectrometry and Gas-Phase Chemistry of Bismuth–Oxido Clusters, *ChemPlusChem*, 2013, **78**, 1005–1014.

58 A. Morgenstern, R. Thomas, O. Selyshchev, M. Weber, C. Tegenkamp, D. R. T. Zahn, M. Mehring and G. Salvan, Anchoring Atomically Precise Chiral Bismuth Oxido Nanoclusters on Gold: The Role of Amino Acid Linkers, *Langmuir*, 2024, **40**, 16320–16329.

59 J. N. Wacker, A. S. Ditter, S. K. Cary, A. V. Murray, J. A. Bertke, G. T. Seidler, S. A. Kozimor and K. E. Knope, Reactivity of a Chloride Decorated, Mixed Valent $CeIII/IV_{38}$–Oxo Cluster, *Inorg. Chem.*, 2022, **61**, 193–205.

60 A. Blanes-Díaz, M. Shohel, N. T. Rice, I. Piedmonte, M. A. McDonald, K. Jorabchi, S. A. Kozimor, J. A. Bertke, M. Nyman and K. E. Knope, Synthesis and Characterization

of Cerium-Oxo Clusters Capped by Acetylacetonate, *Inorg. Chem.*, 2024, **63**, 9406–9417.

61 E. Bêche, P. Charvin, D. Perarnau, S. Abanades and G. Flamant, Ce 3d XPS investigation of cerium oxides and mixed cerium oxide ($Ce_xTi_yO_z$), *Surf. Interface Anal.*, 2008, **40**, 264–267.

62 M. C. Wasson, X. Zhang, K.-i. Otake, A. S. Rosen, S. Alayoglu, M. D. Krzyaniak, Z. Chen, L. R. Redfern, L. Robison, F. A. Son, Y. Chen, T. Islamoglu, J. M. Notestein, R. Q. Snurr, M. R. Wasielewski and O. K. Farha, Supramolecular Porous Assemblies of Atomically Precise Catalytically Active Cerium-Based Clusters, *Chem. Mater.*, 2020, **32**, 8522–8529.

63 J. P. Holgado, R. Alvarez and G. Munuera, Study of CeO_2 XPS spectra by factor analysis: reduction of CeO_2, *Appl. Surf. Sci.*, 2000, **161**, 301–315.

64 A. Vogler and H. Kunkely, Excited state properties of lanthanide complexes: Beyond ff states, *Inorg. Chim. Acta*, 2006, **359**, 4130–4138.

65 H. Tsurugi and K. Mashima, Renaissance of Homogeneous Cerium Catalysts with Unique Ce(IV/III) Couple: Redox-Mediated Organic Transformations Involving Homolysis of Ce(IV)–Ligand Covalent Bonds, *J. Am. Chem. Soc.*, 2021, **143**, 7879–7890.

66 G. Li, K. Kaneko and S. Ozeki, Chemisorption and Photoadsorption of NO on Cerium(IV) Oxide, *Langmuir*, 1997, **13**, 5894–5899.

67 A. N. Gaiser, C. Celis-Barros, F. D. White, M. J. Beltran-Leiva, J. M. Sperling, S. R. Salpage, T. N. Poe, D. Gomez Martinez, T. Jian, N. J. Wolford, N. J. Jones, A. J. Ritz, R. A. Lazenby, J. K. Gibson, R. E. Baumbach, D. Páez-Hernández, M. L. Neidig and T. E. Albrecht-Schönzart, Creation of an unexpected plane of enhanced covalency in cerium(III) and berkelium(III) terpyridyl complexes, *Nat. Commun.*, 2021, **12**, 7230–7239.

68 A. Zając, P. Solarz, M. Ptak, J. Lorenc, S. M. Kaczmarek, G. Leniec, K. Hermanowicz and J. Hanuza, Synthesis, optical and magnetic studies of cerium and europium phytate complexes - new microporous materials, *J. Mol. Struct.*, 2021, **1233**, 130114.

69 M. D. Walter, C. H. Booth, W. W. Lukens and R. A. Andersen, Cerocene Revisited: The Electronic Structure of and Interconversion Between $Ce_2(C_8H_8)_3$ and $Ce(C_8H_8)_2$, *Organometallics*, 2009, **28**, 698–707.

70 R. M. Rakhmatullin, V. V. Semashko, S. L. Korableva, A. G. Kiiamov, A. A. Rodionov, R. Tschaggelar, J. A. van Bokhoven and C. Paun, EPR study of ceria nanoparticles containing different concentration of Ce^{3+} ions, *Mater. Chem. Phys.*, 2018, **219**, 251–257.

71 S. K. Cary, M. G. Ferrier, R. E. Baumbach, M. A. Silver, J. Lezama Pacheco, S. A. Kozimor, H. S. La Pierre, B. W. Stein, A. A. Arico, D. L. Gray and T. E. Albrecht-Schmitt, Monomers, Dimers, and Helices: Complexities of Cerium and Plutonium Phenanthrolinecarboxylates, *Inorg. Chem.*, 2016, **55**, 4373–4380.

72 O. M. Bordun, I. I. Kukharskii, V. V. Dmitruk, V. G. Antonyuk and V. P. Savchin, Luminescence centers in α-Bi_2O_3 ceramics, *J. Appl. Spectrosc.*, 2008, **75**, 681–684.

73 T.-K. Tseng, J. Choi, D.-W. Jung, M. Davidson and P. H. Holloway, Three-Dimensional Self-Assembled Hierarchical Architectures of Gamma-Phase Flowerlike Bismuth Oxide, *ACS Appl. Mater. Interfaces*, 2010, **2**, 943–946.

74 Z. Zhao, L. Wang, G. Zhan, Z. Liu, Z. Bian and C. Huang, Efficient rare earth cerium(III) complex with nanosecond d−f emission for blue organic light-emitting diodes, *Natl. Sci. Rev.*, 2021, **8**, nwaa193.

75 R. Génois, S. Jobic, G. Ouvrard, F. Massuyeau and R. Gautier, The crucial impact of cerium reduction on photoluminescence, *Appl. Mater. Today*, 2020, **20**, 100643.

76 S. Eslava, A. C. Papageorgiou, S. K. Beaumont, G. Kyriakou, D. S. Wright and R. M. Lambert, Synthesis, characterization, and surface tethering of sulfide-functionalized Ti_{16}-oxo-alkoxy cages, *Chem. Mater.*, 2010, **22**, 5174–5178.

77 L. Zobbi, M. Mannini, M. Pacchioni, G. Chastanet, D. Bonacchi, C. Zanardi, R. Biagi, U. Del Pennino, D. Gatteschi and A. Cornia, Isolated single-molecule magnets on native gold, *Chem. Commun.*, 2005, **12**, 1640–1642.

78 J. Gómez-Segura, J. Veciana and D. Ruiz-Molina, Advances on the nanostructuration of magnetic molecules on surfaces: the case of single-molecule magnets (SMM), *Chem. Commun.*, 2007, 3699–3707.

79 B. A. Watson, M. A. Barteau, L. Haggerty, A. M. Lenhoff and R. S. Weber, Scanning tunneling microscopy and tunneling spectroscopy of ordered hetero- and isopolyanion arrays on graphite, *Langmuir*, 1992, **8**, 1145–1148.

80 I. K. Song, R. B. Shnitser, J. J. Cowan, C. L. Hill and M. A. Barteau, Nanoscale Characterization of Redox and Acid Properties of Keggin-Type Heteropolyacids by Scanning Tunneling Microscopy and Tunneling Spectroscopy: Effect of Heteroatom Substitution, *Inorg. Chem.*, 2002, **41**, 1292–1298.

81 J. Zhang, S. Chang, B. H. R. Suryanto, C. Gong, X. Zeng, C. Zhao, Q. Zeng and J. Xie, Efficient Synthesis of Ir-Polyoxometalate Cluster Using a Continuous Flow Apparatus and STM Investigation of Its Coassembly Behavior on HOPG Surface, *Inorg. Chem.*, 2016, **55**, 5585–5591.

82 F. Yang, G. Kalandia, M. Moors, J. Lorenz, M. Rohdenburg, X.-B. Wang, W. Cao, M. A. Moussawi, D. Volke, R. Hoffmann, J. Warneke, T. N. Parac-Vogt and K. Y. Monakhov, Ligand Substituent Effects on the Electronic Properties of Lindqvist-Type Polyoxometalate Multi-Level-Switches in the Gas Phase, Solution and on Surfaces, *Adv. Mater. Interfaces*, 2024, **11**, 2400411.

83 E. Vogelsberg, M. Moors, A. S. Sorokina, D. A. Ryndyk, S. Schmitz, J. S. Freitag, A. V. Subbotina, T. Heine, B. Abel and K. Y. Monakhov, Solution-Processed Formation of DNA-Origami-Supported Polyoxometalate Multi-Level

Switches with Countercation-Controlled Conductance Tunability, *Chem. Mater.*, 2023, **35**, 5447–5457.

84 M. Moors, I. Werner, J. Bauer, J. Lorenz and K. Y. Monakhov, Multistate switching of scanning tunnelling microscopy machined polyoxovanadate–dysprosium–phthalocyanine nanopatterns on graphite, *Nanoscale Horiz.*, 2024, **9**, 233–237.

85 M. Glöß, R. Pütt, M. Moors, E. Kentzinger, S. Karthäuser and K. Y. Monakhov, Exploring the Ligand Functionality, Electronic Band Gaps, and Switching Characteristics of Single Wells–Dawson-Type Polyoxometalates on Gold, *Adv. Mater. Interfaces*, 2022, **9**, 2200461.

86 R. D. Shannon, Revised effective ionic radii and systematic studies of interatomic distances in halides and chalcogenides, *Acta Crystallogr., Sect. A*, 1976, **32**, 751–767.

87 J. C. A. Boeyens, The Periodic Electronegativity Table, *Z. Naturforsch., B*, 2008, **63**, 199–209.

88 A. D. Stoycheva and S. J. Singer, Stripe Melting in a Two-Dimensional System with Competing Interactions, *Phys. Rev. Lett.*, 2000, **84**, 4657–4660.

89 A. D. Stoycheva and S. J. Singer, Scaling theory for two-dimensional systems with competing interactions, *Phys. Rev. E: Stat., Nonlinear, Soft Matter Phys.*, 2001, **64**, 016118.

90 A. D. Stoycheva and S. J. Singer, Computer simulations of a two-dimensional system with competing interactions, *Phys. Rev. E: Stat., Nonlinear, Soft Matter Phys.*, 2002, **65**, 036706.

91 J. J. Weis, Orientational structure in a monolayer of dipolar hard spheres, *Mol. Phys.*, 2002, **100**, 579–594.

92 P. J. Camp, Structure and phase behavior of a two-dimensional system with core-softened and long-range repulsive interactions, *Phys. Rev. E: Stat., Nonlinear, Soft Matter Phys.*, 2003, **68**, 061506.

93 J. J. Weis, Simulation of quasi-two-dimensional dipolar systems, *J. Phys.: Condens. Matter*, 2003, **15**, S1471.

94 I. Fernández-Torrente, S. Monturet, K. J. Franke, J. Fraxedas, N. Lorente and J. I. Pascual, Long-range repulsive interaction between molecules on a metal surface induced by charge transfer, *Phys. Rev. Lett.*, 2007, **99**, 176103.

95 J. Fraxedas, S. García-Gil, S. Monturet, N. Lorente, I. Fernández-Torrente, K. J. Franke, J. I. Pascual, A. Vollmer, R. P. Blum, N. Koch and P. Ordejón, Modulation of Surface Charge Transfer through Competing Long-Range Repulsive versus Short-Range Attractive Interactions, *J. Phys. Chem. C*, 2011, **115**, 18640–18648.

96 T. N. Ha Nguyen, Y. Paltiel, L. T. Baczewski and C. Tegenkamp, Spin Polarization of Polyalanine Molecules in 2D and Dimer-Row Assemblies Adsorbed on Magnetic Substrates: The Role of Coupling, Chirality, and Coordination, *ACS Appl. Mater. Interfaces*, 2023, **15**, 17406–17412.